

**Photoconductivity measurements of the electronic structure of organic solar cells**

R. A. Street, K. W. Song, and J. E. Northrup  
*Palo Alto Research Center, Palo Alto, California 94304, USA*

S. Cowan  
*Center for Polymers and Organic Solids, University of California at Santa Barbara, Santa Barbara, California 93106, USA*  
 (Received 9 November 2010; published 25 April 2011)

Experimental and theoretical studies of the electronic structure of bulk heterojunction (BHJ) organic solar cells are reported. The photoconductivity spectral response of the solar cells has a weak absorption band extending from the band-gap energy down to  $<1$  eV due to charge-transfer optical excitation at the interface between the polymer and the fullerene. The low-energy absorption indicates an exponential band tail of localized states and an absorption model based on the one-electron joint density of electronic states accounts for the data. Transient photoconductivity measurements of the carrier mobility exhibit a temperature-dependent carrier dispersion. Data analysis for the particular case of transport in the BHJ structure is developed. A multiple trapping model of the dispersive transport is consistent with localized band tail states having a comparable density-of-states distribution to those observed by optical absorption. Theoretical calculations of the density of states including disorder in the  $\pi$ - $\pi$  spacing of the polymer chains also shows exponential band tailing. A density-of-states model is developed from the data and is discussed.

DOI: [10.1103/PhysRevB.83.165207](https://doi.org/10.1103/PhysRevB.83.165207)

PACS number(s): 73.50.Gr, 71.20.Rv, 73.50.Pz

**I. INTRODUCTION**

Bulk heterojunction (BHJ) organic solar cells comprise a phase-separated blend of an electron donor and an electron acceptor.<sup>1</sup> The electronic properties of the BHJ cells are defined by the electronic density of states along with the electronic transport, optical absorption, and recombination mechanisms. Band offsets, carrier mobility, disorder-induced band tail states, and interface states are among the factors that may influence the properties. This paper describes measurements of the photoconductivity spectral response to explore optical transitions at the BHJ interfaces, and transient photoconductivity measurements of carrier mobility and lifetime. Information about the electronic structure is obtained from these measurements and from first-principles theoretical calculations of the density of states in the polymer component of the cell.

When a semiconductor comprises both a conduction band of mobile states and localized band tail or trap states, the density of states (DOS) takes on central importance as the basis for interpretation of many measurements. The DOS connects the analysis of the optical absorption and the dispersive transport that are described here, and is needed to calculate the diode and solar cell properties. The DOS also connects the physical structure with the electronic structure. One of the aims of this paper is to develop a DOS model to account for the data.

There are alternative mechanisms that apply to the optoelectronic properties, which have not been fully resolved, and influence the interpretation of experiments. For example, the optical absorption is influenced by the electron-phonon coupling, the presence of disorder-induced band tail states, and excitonic transitions. In bulk polymers, it is reasonably clear that the exciton energy is large and has significant phonon coupling.<sup>2</sup> At the BHJ interface, there is experimental evidence<sup>3</sup> and theoretical expectation<sup>4</sup> that the charge-transfer exciton has a smaller binding energy and lower oscillator

strength than for bulk excitations because the electron and hole are localized on opposite sides of the interface. The structural disorder of both the polymer and the phenyl C61 butyric acid methyl ester (PCBM) can lead to a band tail in the DOS and the band edges. Two models can be applied, depending on whether the disorder energy is larger or smaller than the phonon coupling energy. A strong-coupling (SC) model applies when the phonon interactions dominate over the disorder potential, and a weak coupling with disorder (WCD) model applies in the reverse case. Given the organic materials and the known structural disorder, it is expected that phonon coupling and localized states are both significant.

The two models lead to different explanations for the electronic transport and the carrier mobility. The SC model accounts for the low mobility by polaron hopping transport,<sup>5</sup> while the WCD model provides a multiple trapping explanation, in which carriers are reasonably mobile beyond a certain energy—the mobility edge—but are repeatedly trapped in band tail states and released to the band edge.<sup>6</sup> It is surprisingly difficult to determine from experiment which model applies. Partly this is because the real situation probably contains both phonon coupling and disorder components, but also accurate values for various parameters, such as the band gap and DOS, are needed to resolve the differences, and current data lacks sufficient precision.

Section II describes theoretical calculations and the experimental results for two types of solar cells. Photoconductivity spectral response measurements of the optical excitation across the interface, transient photoconductivity measurements of the carrier mobility, and theoretical calculations of the DOS are described. The data analysis of the transient photoconductivity for a dispersive transport mechanism is developed. Section III shows that the WCD model accounts for the optical transitions, based on a DOS model developed from the measurements and theory, and on estimates of the interface band gap. The WCD interpretation has support from transient photoconductivity

measurements of the solar cells and also from thin-film transistor data for poly (3-hexylthiophene) (P3HT). Section IV discusses the interface band gap, band offsets, band tail states, and carrier mobility.

## II. EXPERIMENTAL MEASUREMENTS

Measurements were made on P3HT:PCBM and PCDTBT:PC<sub>70</sub>BM solar cells.<sup>7,8</sup> The materials, fabrication, and cell structure are described elsewhere.<sup>9</sup> The photoconductivity spectral response experiment uses a 0.25 m grating spectrometer with a halogen light source. The cell circuit has a load resistor so that the measurement is of photocurrent rather than photovoltage. For most of the data the load resistor is 9 k $\Omega$ , but for very weak absorption it was increased to 100 k $\Omega$ . The voltage across the load is measured with a lock-in amplifier with the monochromatic illumination source chopped at 230 Hz. For measurement of the weak signal below the polymer band gap, it is essential to filter out scattered light from the monochromator. Cutoff filters at 715, 850, and 1000 nm reduce the scattered light sufficiently to measure signals with magnitude  $\sim 10^{-7}$  of the peak signal, and the suppression of scattered light was confirmed by measurements with an infrared absorbing filter. The incident light power is measured with a calibrated silicon photodiode for data at wavelengths below 1100 nm and a Ge photodiode for the longer wavelengths, and the spectrum is normalized to the power. The complete spectrum combines the measurements with the different filters and with the unfiltered source.

The excitation source for transient photoconductivity measurements is a nitrogen pumped dye laser emitting a pulse of <10 ns duration at a wavelength of  $\sim 520$  nm. The current is measured from the voltage drop across a small load resistor, usually either 4 or 10  $\Omega$ , and is recorded on a digital oscilloscope. The illumination intensity is kept as small as possible to avoid space-charge effects. The measurements were made with a  $\sim 1$  Hz pulse rate to allow any trapped charge to disperse, and the current transient is an average of up to 64 measurements.

Variable temperature measurements of both spectral response and transient photoconductivity are made with samples mounted in vacuum on a cold-finger cryostat and cooled with liquid nitrogen.

### A. Photoconductivity spectral response

The low-energy spectral response in solar cell structures measures the optical excitation across the heterojunction interface, directly from the polymer HOMO to the PCBM LUMO. Goris *et al.* applied the technique of Fourier-transform photocurrent spectroscopy (FTPS), originally attributing the low-energy absorption to band tailing in the polymer,<sup>10</sup> but later to the charge-transfer (CT) excitation at the interface.<sup>11</sup> Our measurements of PCDTBT:PC<sub>70</sub>BM also attribute the absorption to excitations directly across the interface. Vandewal recently applied the SC model to a more extensive data set and attributed the subgap absorption to a Gaussian-broadened CT complex.<sup>12</sup> Photothermal deflection spectroscopy (PDS) also measures weak subgap absorption and has been applied to

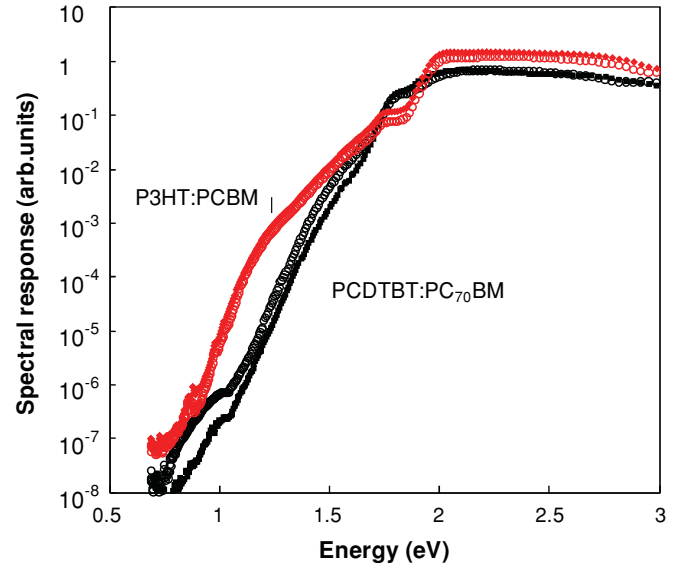


FIG. 1. The photoconductivity spectral response of two P3HT:PCBM and two PCDTBT:PC<sub>70</sub>BM solar cells normalized to the incident light power. The data are made up of several measurements with different optical filters.

BHJ cells.<sup>13</sup> Unlike PDS, techniques based on photoconductivity have the possible advantage of selectively measuring transitions that excite mobile carriers across the interface, which are the excitations of interest for solar cells. Recently Lee *et al.* compared the spectral response of the solar cells with the optical absorption of the cell and the component materials.<sup>14</sup> This work along with Refs. 10 and 11 show that optical absorption extends to lower energy in the blend than in the component materials, which is the primary evidence to assign the absorption to the CT transitions.

Figure 1 shows examples of the spectral response of the two types of solar cells, measured at zero bias voltage and hence effectively under short-circuit conditions, since the voltage drop across the load resistor is less than 10 mV. The complete spectrum is obtained from four to six separate measurements with different optical filters, two different spectrometer gratings, and two photodiodes for intensity calibration. The different data sets agree with good accuracy where they overlap. The spectrum is measured over seven orders of magnitude in photocurrent and measurements of the low-energy region are only possible with careful optical filtering. Different samples show slight changes in the spectrum, probably due to minor variances in the fabrication. Figure 2 shows a set of raw photocurrent data covering the low-energy region showing the response with different filters and also with an infrared absorbing filter. Below 1 eV there is significant background even with an IR absorbing filter due to some residual scattered light. The background is subtracted to obtain the spectrum. The weak signal and presence of scattered light add some uncertainty to the shape of the spectrum in this region. The spectrum is unchanged when the measurements are performed with bias light illumination, in this case using a green light-emitting diode. The spectral response is therefore reasonably unaffected by the recombination kinetics, implying a first-order process down to very low illumination levels.

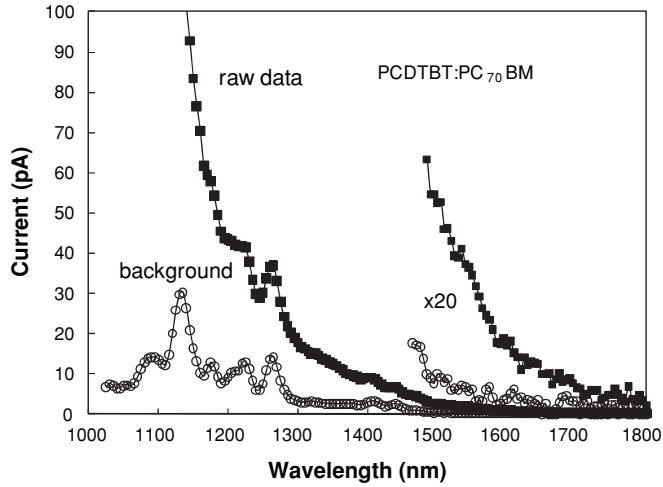


FIG. 2. Raw photoconductivity spectral response measurements with and without an infrared absorbing filter, to show the background which is subtracted to obtain the spectrum.

The response above  $\sim 2$  eV agrees with independent solar cell measurements on the same or similar devices.<sup>15</sup> The response drops in the range 1.8–2 eV corresponding to the bulk optical absorption edges of the component materials. There is a broad shoulder in the spectral response down to 1.2–1.4 eV and then an approximately exponential drop to  $\sim 0.8$  eV in both types of cell. The response of the PCDTBT cell is shifted up in energy by  $\sim 0.2$  eV compared to the P3HT cell.

In common with the other measurements of low-energy photoconductivity and absorption described above, we attribute the photoconductivity spectra to CT excitations across the interface band gap, from the polymer HOMO to the PCBM LUMO. Figure 3 shows a schematic energy diagram of the BHJ structure illustrating the band offset between the two materials.

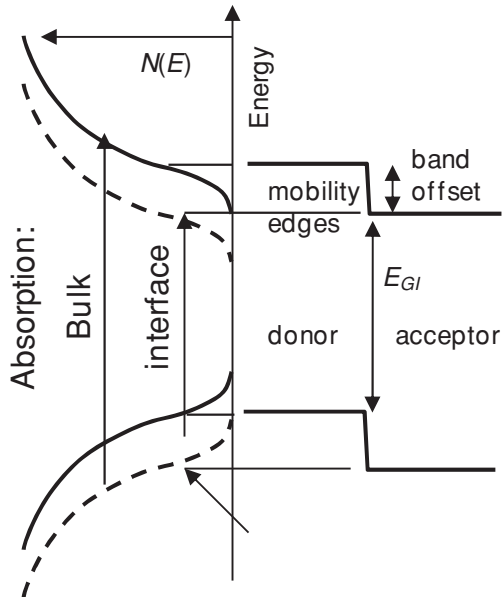


FIG. 3. Schematic band diagram illustrating the band offset, interface band gap  $E_{GI}$ , and distribution of states  $N(E)$  of the component materials. The interface absorption transitions are shown compared to the bulk absorption.

The figure illustrates the energy bands and the interface optical transitions compared to the bulk transitions. The quantum efficiency of free-carrier generation for absorption into the bulk is known to be above 70% in good quality cells and can be close to 100% at short circuit.<sup>15</sup> The direct excitation of electron-hole pairs at the interface should be no less efficient, since it does not require an exciton to migrate to the interface and split. Lee *et al.* compare the room-temperature optical absorption and the photoconductivity spectrum and confirm that the quantum efficiency of the high-energy and low-energy transitions are the same. We make the assumption that the quantum efficiency remains the same at high and low energy over the temperature range of our measurements.

A linear dependence of the photocurrent on light intensity and a quantum efficiency that is approximately independent of photon energy  $\hbar\omega$ , allows a calculation of the optical absorption coefficient  $\alpha_T(\hbar\omega)$  for both the bulk and interface absorption, obtained from the photocurrent  $I_{PC}(\hbar\omega)$ , by

$$I_{PC}(\hbar\omega) = I_0\{1 - \exp[-\alpha_T(\hbar\omega)d]\}, \quad (1)$$

where  $I_0$  is the photoconductivity at complete absorption, and  $d$  is the effective cell thickness, which is twice that actual thickness since there is a metal reflecting layer at the back of the cell. When  $\alpha_T(\hbar\omega)d \ll 1$ , then  $\alpha_T(\hbar\omega)d = I_{PC}/I_0$ . The value of  $I_0$  depends on the recombination processes and hence will vary with sample thickness, temperature, and applied bias. Our analysis uses an experimentally determined value of  $I_0$ . Separate optical transmission measurements of the optical absorption are shown in the inset to Fig. 4, and the value of  $I_0$  is chosen so that the transmission and photoconductivity measurements agree. The calculated optical absorption spectra for the two types of cells are shown in Fig. 4.

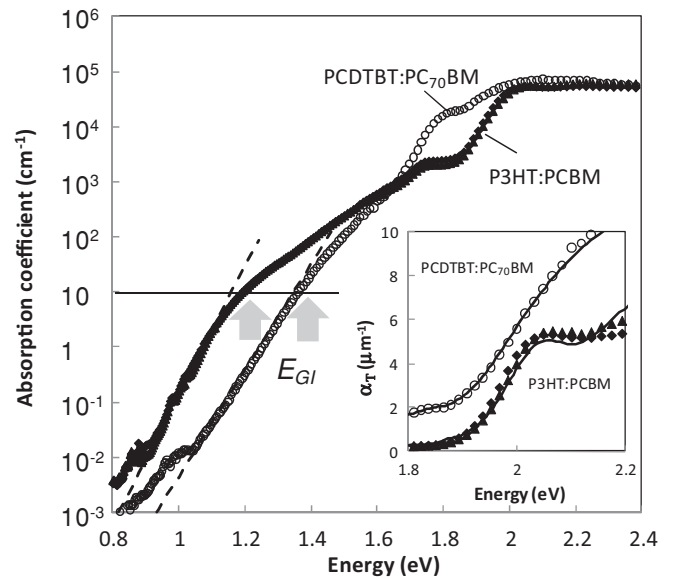


FIG. 4. Optical absorption coefficient  $\alpha_T$  extracted from the data in Fig. 1 for the two types of cell. The vertical arrows indicate the estimated interface optical band gaps  $E_{GI}$  for the two types of cell. The inset shows the absorption coefficient measured by optical transmission on similar samples (solid lines) compared to the absorption obtained from the photoconductivity.

The optical absorption coefficient of both types of cell reaches a plateau of  $\sim 10^5 \text{ cm}^{-1}$  above 2 eV and drops by a factor  $\sim 10$  between 1.8 and 2 eV. The feature near 1.7–1.8 eV is attributed to absorption by PCBM.<sup>12,13</sup> The broad featureless band to low energy, due to the CT absorption, is observed to an absorption coefficient below  $0.01 \text{ cm}^{-1}$ . The initial drop in absorption occurs at  $\sim 1.8 \text{ eV}$  in PCDTBT:PC<sub>70</sub>BM and the CT absorption band is shifted to higher energy as compared to the P3HT cells. Between 0.9 and 1.2 eV the absorption drops exponentially with a slope of 0.037 eV for P3HT:PCBM and 0.045 eV for PCDTBT:PCBM (see Fig. 4), characteristic of a typical Urbach absorption edge in disordered materials.<sup>16</sup> The Urbach edge is described by

$$\alpha_T(\hbar\omega) = \alpha_0 \exp\left(\frac{\hbar\omega - E_{\text{GI}}}{E_0}\right), \quad \hbar\omega \leq E_{\text{GI}}, \quad (2)$$

where  $E_0$  is the slope of the exponential tail,  $E_{\text{GI}}$  is the interface band gap as illustrated in Fig. 3, and  $\alpha_0$  is the optical absorption coefficient at the energy  $E_{\text{GI}}$ .

In both types of cell, the absorption is detectable to 0.3–0.4 eV below the CT band gap (see Fig. 4). Despite the uncertainty in the exact value of  $E_{\text{GI}}$ , it seems clear that excitations well below the interface gap can excite photoconductivity. An obvious explanation is the presence of a significant band tail in the DOS that describes the CT transitions. The optical absorption corresponds to excitations from the band tail to the opposite band, and such transitions excite photoconductivity provided the band tail carrier is thermally excited to a mobile state. Even though the SC model attributes the absorption to strong phonon coupled excitations, the observation of absorption well below the gap suggests band tailing even within this model.

There are some additional features and a change of slope at low absorption coefficients,  $< 0.1 \text{ cm}^{-1}$ . This is the region where the signal is very small and may be susceptible to noise and scattered light. The data suggest optical transitions through deeper states, but further measurements are needed to confirm the structure in this region before there is a more detailed interpretation of the data.

Figure 5 shows the photoconductivity spectral response for the PCDTBT cell at temperatures from 190 to 330 K. The peak photoconductivity decreases by approximately a factor of 2 at low temperature due to an increasing component of recombination at short circuit, which is reflected in lower values of  $I_0$  in Eq. (1). The results are therefore plotted as relative values scaled to show the individual data sets. The response at 1.7–1.8 eV shows a steeper drop below the PCBM feature at low temperature, indicative of a sharper absorption edge. When the data is scaled to the same peak value, they overlap in the energy range 1.4–1.6 eV, showing that there is virtually no change in the absorption. The exponential absorption in the range 1.1–1.4 eV becomes slightly steeper at low energy, as shown in more detail in Fig. 6, with a change in slope of  $\sim 0.01 \text{ eV}$  over the temperature range. The P3HT cell data is similar. There is a small but significant shift of the spectrum to higher energy in the energy range of the interface gap, and also at the main absorption band near 2 eV. The exponential tail at low energy also gets steeper at low temperature. The inset to Fig. 6 shows the temperature dependence of the exponential slope for both types of cells.

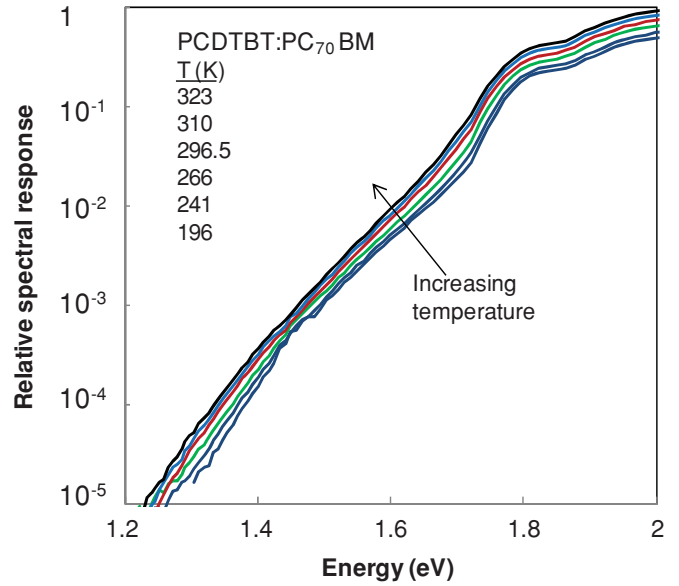


FIG. 5. Temperature dependence of the photocurrent spectral response of the PCDTBT cell. Data are offset vertically for clarity.

The temperature dependence of the exponential edge is typical of an Urbach edge in a disordered material, for which the exponential slope is a combination of static and thermal disorder broadening.<sup>17</sup> As discussed below, we associate the slope of the exponential with the shape of the band tail DOS. The temperature dependence of  $E_0$  can be explained

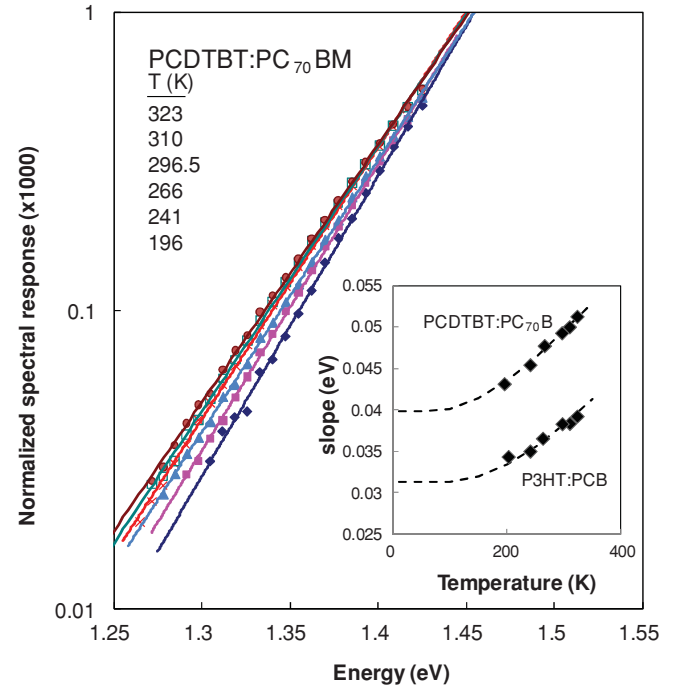


FIG. 6. Detail of the temperature dependence of the photoconductivity spectral response of PCDTBT in the region of the low absorption exponential tail. The inset shows the exponential slope  $E_0$  as a function of temperature for both P3HT and PCDTBT cells. The dashed lines are fits to the model of Eq. (3) comprising a static and thermal component as discussed in the text.



by thermal broadening and the dashed lines in the inset to Fig. 6 show a simple Einstein model to account for the observations,<sup>17</sup>

$$E_0 = E_S + k\Theta[\exp(\Theta/T) - 1]^{-1}. \quad (3)$$

The static component  $E_S$  is indicated from the low-temperature limit of  $E_0$  in Fig. 6 and the thermal components correspond to characteristic temperatures of  $\Theta = 500$  and 650 K for the PCBTBT and P3HT cells, respectively.

### B. Transient photoconductivity

Transient photoconductivity measures the sweepout of charge from the device and provides a measure of the mobility from the carrier transit time. The time-of-flight (TOF) technique is widely used to measure the mobility of low-mobility materials, and has been applied to organic semiconductors.<sup>18</sup> McNeill and Greenham measure the TOF mobility in P3HT and polymer blends.<sup>19</sup> The hole mobility is found to be  $6 \times 10^{-5} \text{ cm}^2/\text{V s}$  in the single material and two to three times lower in the blend, and is dispersive in both cases. The mobility is measured in the perpendicular to the substrate, in contrast to the geometry for thin-film transistors, where the mobility is usually much larger. Choulis *et al.* find a slightly larger mobility for the same perpendicular geometry, but more dispersion.<sup>20</sup> TOF measurements have also been made on P3HT:PCBM solar cells using a very small contact area to increase the time response. The response time at  $< 1 \mu\text{s}$  was analyzed in terms of a hole mobility of  $2 \times 10^{-4} \text{ cm}^2/\text{V s}$  and electron mobility of  $2 \times 10^{-3} \text{ cm}^2/\text{V s}$ .<sup>21</sup>

The mobility dispersion, described by a power-law time dependence of the mobility, is of particular interest because in many disordered materials the dispersion is related to the density of localized states near the band edge.<sup>22</sup> Figure 7 shows the room-temperature transient photoconductivity for

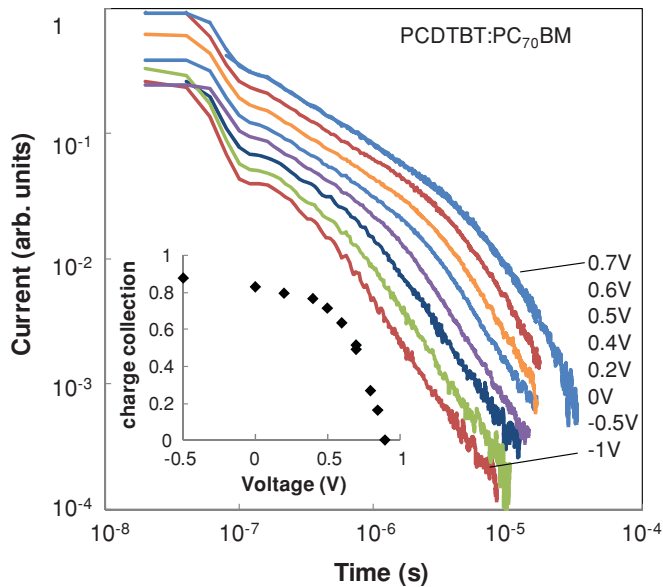


FIG. 7. Transient photoconductivity measurements at room temperature for a PCDTBT:PCBM cell, for different bias voltages as shown. The transit of the faster carrier is complete by  $0.1 \mu\text{s}$  and the later response is due to the slower carrier. The inset shows the bias dependence of the charge collection  $Q(V)$ .

PCDTBT cells as a function of bias voltage. The figures also show the integrated charge collection  $Q(V)$  as a function of voltage.<sup>23</sup> The charge collection approaches a constant in reverse bias because all the mobile charge is collected at the electrodes, and decreases in forward bias due to recombination. The measurements of  $Q(V)$  show that the transient data for the bias voltages used in Fig. 7 have a charge collection of  $> 50\%$  and so are dominated by carrier sweepout, allowing us to determine the mobility from the transit times. The comparable data for a P3HT cell is discussed below.

The transient photoconductivity contains the sum of the response from electrons and holes, because the cells are sufficiently thin that optical absorption of the excitation pulse occurs throughout the sample. The response of the faster carrier is observed in the data for both cells as the larger photocurrent at short times. In PCDTBT cells the fast response extends to only  $0.1 \mu\text{s}$ , and is limited by the  $RC$  time constant of the electronics. In P3HT cell the faster carrier response extends further and significantly overlaps the response of the slower carrier, particularly at low bias voltages where the slow response extends to  $\sim 1 \mu\text{s}$ . The slower carrier has a response that approximates to two power-law regions, which is characteristic of dispersive transport with the change of slope identifying the transit time.

Elsewhere we show that the transient photocurrent  $I_P(t, V)$  for nondispersive transport is the sum of contributions for electrons and holes, given by<sup>24</sup>

$$I_{Pi}(t, V) = (N_0 e \mu_i V_i / d) \exp(-t/\tau_{Ri}) (1 - \mu_i V_i t / d^2), \quad i = n, p, \quad (4)$$

where  $N_0$  is the initial mobile carrier concentration,  $\mu$  is the mobility,  $V_i$  is the internal voltage,  $\tau_R$  is the lifetime,  $d$  is the sample thickness,  $e$  is the electronic charge, and the subscripts  $n$  and  $p$  refer to the transport of electrons and holes. Equation (4) applies when the carriers are created uniformly throughout the thickness of the device, and so applies to BHJ cells where the absorption depth is similar to or greater than the device thickness. The first term  $(N_0 e \mu V_i / d)$  on the right-hand side of Eq. (4) is the initial photocurrent summed over all the mobile carriers in the device. The second term  $[\exp(-t/\tau_R)]$  corresponds to the loss of carriers by deep trapping or recombination and the third term  $(1 - \mu V_i t / d^2)$  is the loss of carriers that reach the electrode. This term arises because the transit time varies from zero to  $d^2/\mu V_i$ , for carriers created near the collection electrode and at the opposite electrode, respectively. Equation (4) also makes the approximation that the internal field is uniform, and hence that space-charge effects are negligible.

The analysis must be modified when the transport is dispersive. The constant mobility is replaced with a time-dependent one,  $\mu_0 t^{\alpha-1}$ , where  $\alpha$  is the dispersion parameter, and the current at the transit time does not drop to zero. According to the standard model of dispersive transport,<sup>25</sup> the photocurrent  $I_P(t)$  resulting from charge created at the opposite side of the sample from the collection electrode is given by

$$I_P(t) = N_0 e \mu_0 t^{\alpha-1} E \quad \text{for } t < T, \quad (5)$$

$$I_P(t) = I_P(T) t^{-\alpha-1} \quad \text{for } t > T, \quad (6)$$

where  $T$  is the transit time given by

$$\int_0^T \mu_0 E t^{\alpha-1} dt = d, \quad T = (\alpha d / \mu_0 E)^{1/\alpha}. \quad (7)$$

When charge is excited at distance  $x$  from the collection electrode, the contribution from an element of charge of width  $dx$  becomes

$$I_P(t, x) dx = N(x) dx e \mu_0 t^{\alpha-1} E \quad \text{for } t < T(x), \quad (8)$$

where  $N(x)$  is the profile of optically excited carriers and

$$I_P(t, x) dx = I_P(T, x) t^{-\alpha-1} \quad \text{for } t > T(x), \quad (9)$$

$$T(x) = (\alpha x / \mu_0 E)^{1/\alpha}, \quad (10)$$

$$I_P(t) = \int_0^d I_P(t, x) dx. \quad (11)$$

The total photocurrent is the sum of separate contributions for the electron and hole, each of which has the same  $N(x)$  since the electrons and holes are created together. These expressions neglect deep trapping or recombination, which can be included by adding the same  $\exp(-t/\tau_R)$  term as in Eq. (4). However, the trapping may not have an exponential dependence on time in the case of dispersive transport. The experiments cover bias voltages for which the charge collection is high and hence trapping lifetime effects are not significant.

Figure 8 shows the photocurrent model described by Eqs. (8)–(11) for different values of the dispersion parameter and assuming a uniform carrier profile, such that  $N(x)$  is a constant. The figure also compares the model with the standard dispersive transport case [Eqs. (5)–(7)] under the condition that

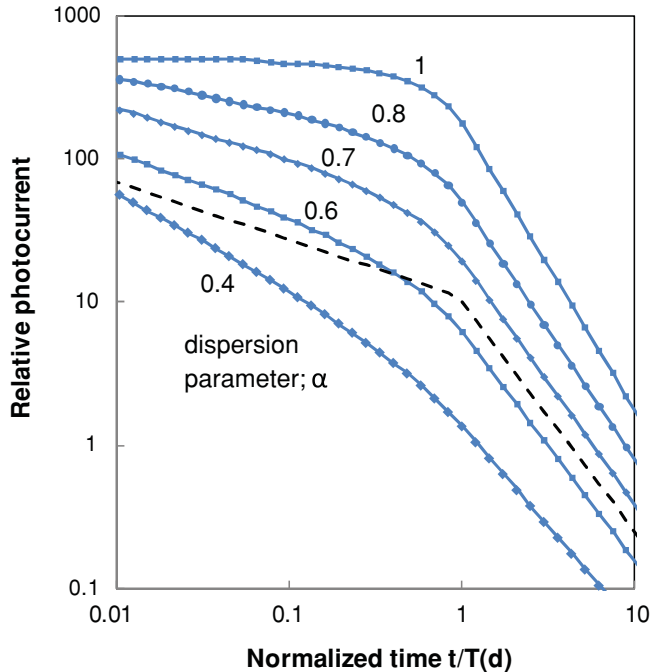


FIG. 8. Calculations of dispersive transport given by Eqs. (8)–(11), for different values of the dispersion parameter  $\alpha$ , and with normalized transit times  $T(d)$  as described in the text. For comparison, the dashed line shows the standard dispersive transport model, for carriers that completely cross the sample, with  $\alpha = 0.6$ .

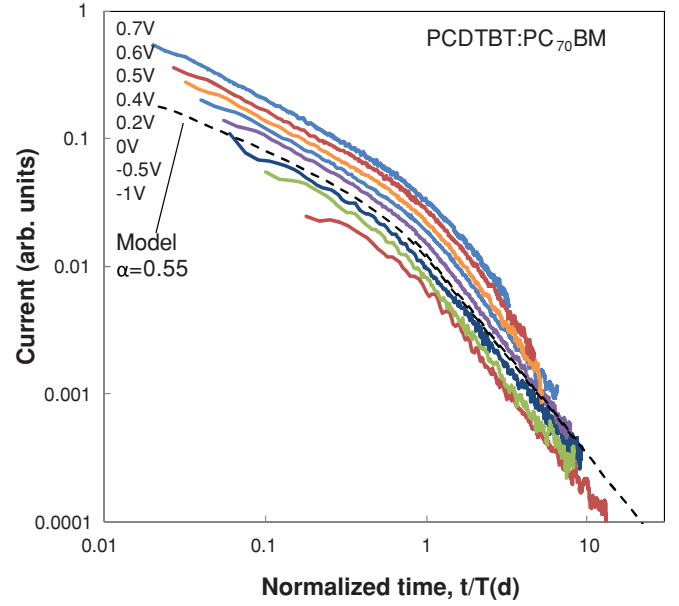


FIG. 9. The transient photoconductivity data of PCDTBT:PCBM, from Fig. 7, with the time scaled to correspond to the normalized transit time  $T(d)$ . The dashed line is the model of Fig. 8 with dispersion parameter  $\alpha = 0.55$ .

all the carriers completely cross the sample. The model uses a normalized time scale to give a transit time of  $T(d) = 1$ . The current drops before the transit time more rapidly than in the standard model because carriers that are generated in the middle of the sample have shorter transit times than  $T(d)$ . Hence, the change of slope separating the short- and long-time behavior occurs at a time less than  $T(d)$ , and the photocurrent time dependence is not the power law of the ideal dispersive transport model. The similarity between the model and the measured data is evident.

Figure 9 compares the model to the PCDTBT data in Fig. 7. The data are scaled in time to give a transit time  $T(d) = 1$  as in the model, with a different scaling factor for each voltage. The value of the dispersion parameter,  $\alpha = 0.55 \pm 0.05$ , is chosen to give the best fit to the whole data set. Data are offset vertically to show the individual measurements. Small values of  $V_{BI} - V$  give most information about the photocurrent before the transit time and large values tell more about after the transit time. The results give a consistent fit, in part because the response of the faster carrier occurs at short enough times that it does not interfere with the response of the slower carrier. The scaling factors in time provide the actual values of the transit time, which are plotted in Fig. 10 as a function of inverse internal voltage. The line in Fig. 10 corresponds to a mobility of  $1.4 \times 10^{-4} \text{ cm}^2/\text{V s}$  for an estimated cell thickness of 130 nm, and the departure from the linear relation at large values of inverse voltage is expected as the probability of recombination or deep trapping increases. Dispersive transport predicts that the mobility decreases as the transit time increases, and it is often suggested that the mobility in polymers is field dependent. However, no field dependence is apparent in the data, perhaps because of the limited range of the electric field.

Figure 11 shows the equivalent data for the P3HT cell. In this case, the response of the faster carrier overlaps more

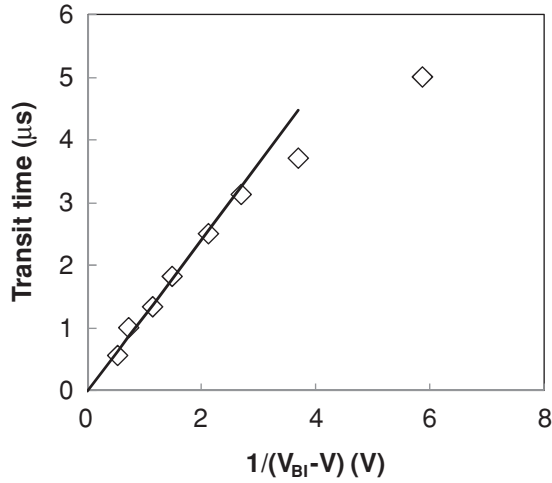


FIG. 10. Plot of the carrier transit time vs the inverse of the internal voltage for the PCDTBT:PCBM cell data in Figs. 7 and 9. The internal voltage is the difference between the built-in potential  $V_{BI}$  and the applied voltage  $V$ . The solid line through the data corresponds to a mobility of  $1.4 \times 10^{-4} \text{ cm}^2/\text{V s}$ .

with the slower carrier, and so the quality of the fit is poorer. Better data is needed to extract both components of the transient simultaneously. We estimate a dispersion parameter of  $0.75 \pm 0.1$ .

Figures 12 and 13 show the transient photoconductivity in the two types of cell at different temperatures ranging from 200 to 330 K for a fixed bias voltage. The slopes of the data

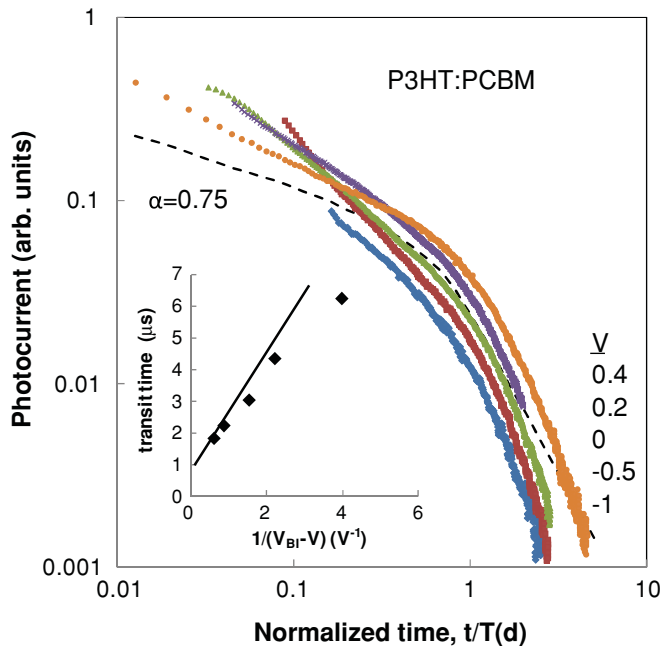


FIG. 11. (Color online) The transient photoconductivity data of P3HT:PCBM, at the voltages indicated, with the time scaled to correspond to the normalized transit time. The dashed line is the model of Fig. 8 with dispersion parameter  $\alpha = 0.75$ . The inset is a plot of the carrier transit time vs the inverse of the internal voltage, the difference between the built-in potential  $V_{BI}$  and the applied voltage  $V$ .

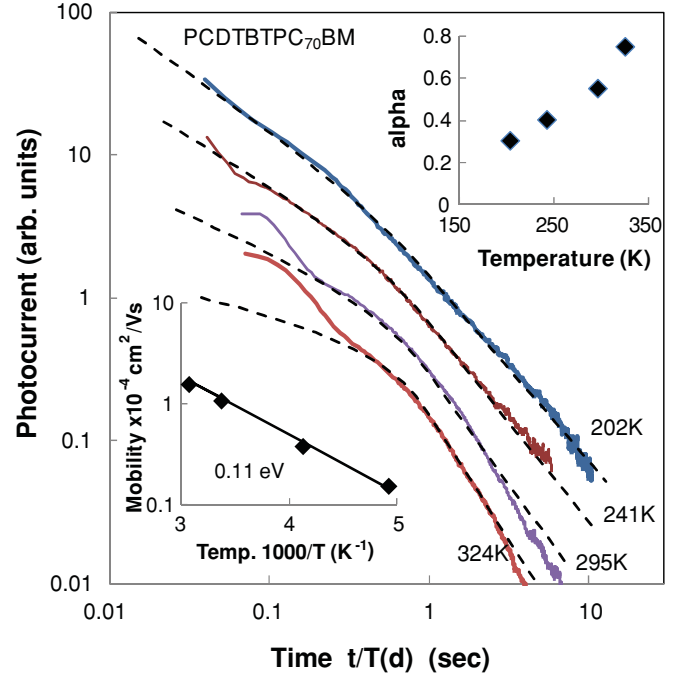


FIG. 12. (Color online) Transient photoconductivity measurements for a PCDTBT:PCBM cell at different temperatures and a fixed bias voltage of 0.4 V, compared to fits to the dispersion model of Fig. 8 (dashed lines). The upper inset shows the temperature dependence of the dispersion parameter  $\alpha$  and the lower inset shows the carrier mobility as a function of inverse temperature, indicating that the mobility has an activation energy of 0.11 eV.

before and after the transit time show that there is increasing dispersion at low temperature. The mobility and dispersion parameter are obtained by the same method of scaling the data to  $T(d) = 1$  and matching the data and model. The best fits are shown in the figures. The fit of the P3HT data improves at low temperature probably because the response of the faster carrier has less time overlap with the slower carrier. The estimated dispersion parameters, which decrease at low temperature, and the temperature dependence of the mobility are shown in the insets to Figs. 12 and 13. The measured mobility approximates to the empirical form

$$\mu = \mu_0 \exp(-E_T/kT). \quad (12)$$

For P3HT, the mobility prefactor  $\mu_0$  is  $\sim 0.1 \text{ cm}^2/\text{V s}$ , and the transport activation energy  $E_T$  is 0.17 eV. For PCDTBT the mobility prefactor is  $0.01 \text{ cm}^2/\text{V s}$ , and the transport activation energy is 0.11 eV.

A common mechanism for carrier dispersion is multiple trapping in an exponential distribution of band tail states proportional to  $\exp[-(E - E_M)/E_{T0}]$ , where  $E_M$  is the energy of the mobility edge and  $E_{T0}$  is the band tail slope.<sup>26</sup> The model assume a mobility edge separating mobile and trapping states and that carriers are thermally excited from the traps to the mobile states. This model predicts dispersive transport, provided that  $E_{T0} > kT$ , with

$$\alpha = kT/E_{T0}. \quad (13)$$

Within this model, the transient photocurrent measurements give values of  $E_{T0}$  of  $\sim 0.045 \pm 0.005 \text{ eV}$  and  $\sim 0.033 \pm 0.007 \text{ eV}$

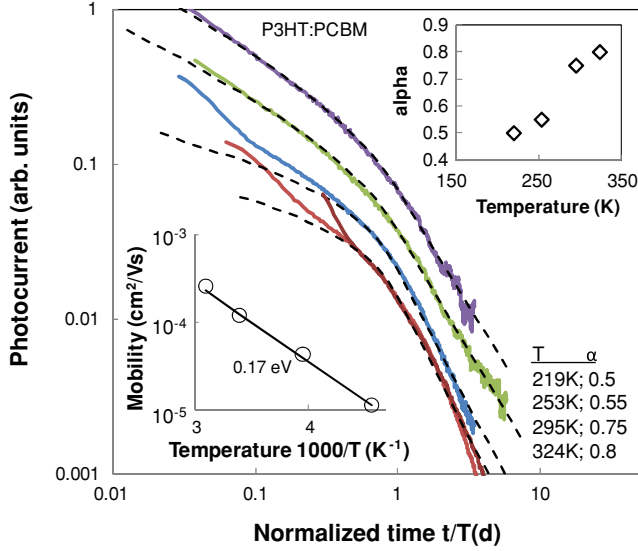


FIG. 13. Transient photoconductivity measurements for a P3HT:PCBM cell at different temperatures and a fixed bias voltage of 0.4 V, compared to fits to the dispersion model of Fig. 8 (dashed lines). The insets show the temperature dependence of the dispersion parameter and of the carrier mobility as in Fig. 12.

for the PCDTBT and P3HT cells, respectively, based on the room-temperature measurements of  $\alpha$ . These values of  $E_{T0}$  are the same within experimental uncertainty as the exponential slope  $E_0$  observed for the low-energy optical absorption, showing that exponential band tails provide a consistent explanation of both experiments. The temperature dependence of the dispersion parameter, which shows that  $\alpha$  increases with temperature, is also consistent with Eq. (13), although the temperature dependence deviates significantly from the model for the PCDTBT cell. The thermal activation of the mobility is also consistent with the model, and the activation energy is an average over the distribution of traps.

The model for the mobility and dispersion implicitly assumes that the carriers move perpendicular to the plane of the cell. In practice, the cell structure is disordered and the actual path length from one contact to the other may be greater than the thickness of the cell and distributed, but the details are not known. A longer path length increases the calculated mobility and the variation in path length may contribute to the dispersion.

### C. Calculations of the density of states

Calculations were performed in order to obtain a theoretical estimate of the distribution of band tail states in P3HT. P3HT has a polycrystalline structure with polymer chains in a  $\pi$ -stacked configuration, forming lamella separated by the alkyl chains.<sup>27</sup> The equilibrium distance between neighboring conjugated chains is 3.8 Å. However, there is a distribution of distances arising from static disorder that has been observed by x-ray diffraction. The calculation is based on the assumption that the tail states arise from fluctuations in the  $\pi$ -stacking distance. We therefore assume a Gaussian distribution of  $\pi$ -stacking distances having a standard deviation  $\sigma$  relative to the average spacing. The value of  $\sigma$  for P3HT is not known,

but we expect it to be similar to the value obtained recently by Rivnay and co-workers for poly[2,5-bis(3-alkylthiophen-2-yl)thieno(3,2-b)thiophene] (PBTBT) using x-ray scattering ( $\sigma_{\text{PBTBT}} \sim 0.06$ ).<sup>28</sup> A model crystallite is generated containing 50 chains with a distribution of distances consistent with the Gaussian distribution. The DOS is determined by calculation of the spectrum for such systems and averaging the results over an ensemble of 8000 crystallites.

The calculation of the spectrum is based on a simple tight-binding model for the highest occupied band. In crystalline-ordered P3HT density functional calculations have shown that this band exhibits an energy dispersion of  $\sim 2.0$  eV along the conjugated chain, and a dispersion of  $\sim 0.6$  eV in the  $\pi$ -stacking direction.<sup>29</sup> The simplest model Hamiltonian that can describe this band has one orbital per cell, with hopping matrix elements  $h$  connecting neighboring cells along the chain and matrix elements  $t$  connecting neighboring chains in the  $\pi$ -stacking direction. In our model  $h$  is a constant equal to 0.5 eV and  $t$  depends only on the distance between neighboring chains,

$$t(d) = t_0 \exp[-\beta(d - d_0)]. \quad (14)$$

The functional form of  $t(d)$  and the values for  $t_0$  and  $\beta$  are determined from density functional pseudopotential calculations for systems containing four conjugated chains per supercell. The energy bands are calculated as discussed elsewhere,<sup>29</sup> for structural configurations with various displacements of the conjugated chains along the  $\pi$ -stacking direction. The P3HT chains are tilted by  $\sim 23^\circ$ .<sup>30</sup> We consider sets of displacements having the pattern  $(0, \Delta d, 0, -\Delta d)$  for the four chains. In these calculations the energy of the highest occupied state ( $E_{\text{vbm}}$ ) depends on  $\Delta d$  and increases from  $E_{\text{vbm}} = 0$  for  $\Delta d = 0$  to  $E_{\text{vbm}} = 0.073$  eV for  $\Delta d = 0.29$  Å and  $E_{\text{vbm}} = 0.155$  eV for  $\Delta d = 0.41$  Å. From calculations employing various values of  $\Delta d$  we show that the exponential dependence of  $t$  on  $d$  is a good approximation, and obtain  $t_0 = 0.15$  eV and  $\beta = 2.4 \text{ Å}^{-1}$ .

We then determine the spectrum of a matrix  $\mathbf{H}$  with off-diagonal matrix elements connecting neighboring states along the conjugated chain ( $h$ ) and in the  $\pi$ - $\pi$  stacking direction ( $t$ ). For a system with 50 chains and 20 monomers per chain this corresponds to a  $N \times N$  Hamiltonian matrix with  $N = 1000$ . The off-diagonal matrix elements  $t = t(d)$  are obtained by employing a Gaussian distribution of values  $(d - d_0)$  with a standard deviation  $\sigma$ . The density of states obtained from these calculations is shown in Fig. 14.

Results for the DOS distribution are shown in Fig. 14 and correspond to four different values of  $\sigma$ . The calculations find that there is an exponential DOS beyond the band edge in the presence of disorder. The slope of the exponential band tails ranges from 10 to 170 meV for the values of  $\sigma$  shown in the figure. A band tail slope of 40 meV corresponds to  $\sigma \sim 0.04$ – $0.05$ , which is close to the experimental value for PBTBT. Thus the exponential band tails indicated by the experimental measurements are supported by the theoretical calculations.

### III. ANALYSIS AND DENSITY OF STATES MODEL

The Urbach optical absorption tail, the dispersive transport, and the calculations of the electronic structure are all consistent with an exponential distribution of disorder-induced band tail



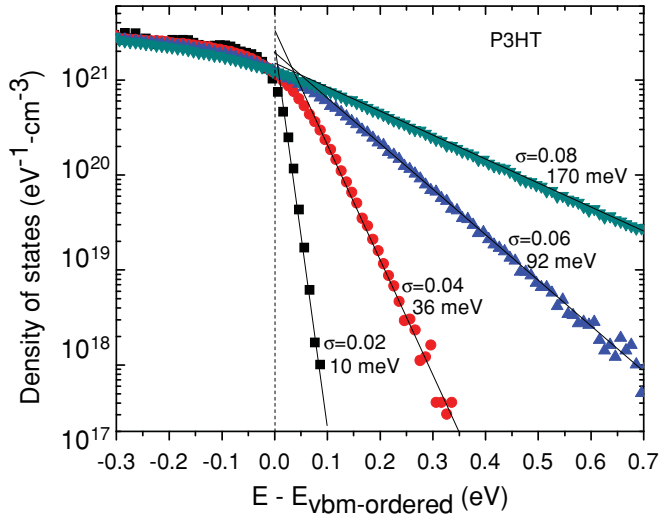


FIG. 14. Calculation of the DOS for P3HT for different assumed levels of  $\pi$ - $\pi$  stacking disorder as a function of energy from the valence-band maximum  $E_{vbm}$ . A tight-binding model with parameters obtained from density functional pseudopotential calculations was employed as described in the text. The standard deviation,  $\sigma$ , of the  $\pi$ -stacking spacing and slope of the exponential tails for the four data sets are indicated. The standard deviation  $\sigma$  is given as a ratio to the nominal  $\pi$ - $\pi$  stacking distance.

states in either or both of the polymer HOMO or the PCBM LUMO. Exponential band tails are typical of disordered semiconductors,<sup>31</sup> and are the basis for models of organic thin-film transistors fabricated from the same polymer materials as used in the solar cells.<sup>32</sup> In this section we develop an approximate DOS model and show in further detail how it accounts for the various experiments.

The DOS depends on assumed physical mechanisms. Thus, we interpret the interface absorption in terms of a weak-coupling model and the mobility in terms of multiple trapping. The multiple trapping model is widely adopted for polymer thin-film transistors (TFTs). Structural measurements show that polymers such as the thiophenes form highly textured polycrystalline films with small grain size. This structure naturally fits the multiple trapping model, with the grains providing the conduction path, and the grain boundaries the trapping states. The structure of the BHJ cells is less well understood and the transport path is different, being out of plane in the solar cells and in plane in the TFTs. The polymers probably form a similar polycrystalline structure as in the TFTs, while the crystallinity of the PCBM is still unclear.

#### A. The interface band gap

The DOS and further analysis of the CT absorption obtained from the photocurrent spectral response needs a value for the interface band-gap energy. Various estimates place the P3HT HOMO between  $\sim 4.8$  and  $5.2$  eV and the PCBM LUMO near  $3.8$  eV with comparable variation,<sup>33</sup> giving an interface band-gap energy of  $\sim 1.2$  eV in P3HT:PCBM but with considerable uncertainty.

Another, perhaps more accurate, method to estimate the interface gap is from the expected relation between the open-

circuit voltage  $V_{OC}$  and the electron and hole quasi-Fermi energies  $E_{qFi}$  ( $i = n, p$ ),

$$V_{OC} = E_{GI} - E_{qFn} - E_{qFp}. \quad (15)$$

The position of the quasi-Fermi energies for PCDTBT cells at 1-sun illumination are estimated to be  $0.25$ – $0.3$  eV based on the recombination lifetime,<sup>34</sup> and the transient photoconductivity data show that P3HT has a similar recombination lifetimes and hence a similar value of  $E_{qF}$ . The quasi-Fermi energies depend only logarithmically on the various parameters and  $E_{GI} - V_{OC}$  is typically found to be  $0.5$ – $0.6$  eV in many solar cells. The P3HT cells have a 1-sun  $V_{OC}$  of  $0.6$ – $0.65$  V, giving an estimate of  $\sim 1.2$  eV for the interface gap. The agreement between the two estimates gives reasonable confidence in the value of  $E_{GI}$  and  $1.2$  eV is also close to the start of the exponential tail to the optical absorption in Fig. 4, which is another indicator of the gap.

Using the  $1.2$ -eV estimate, the interface band gap of the P3HT cell therefore corresponds to an absorption coefficient of  $\alpha_T(E_{GI}) \sim 10 \text{ cm}^{-1}$  for the data in Fig. 4. The CT absorption band is shifted up in energy by  $0.15$ – $0.2$  eV in the PCDTBT cell. The shift is consistent with the increase in the 1-sun open-circuit voltage to  $0.8$ – $0.85$  V, which is also  $\sim 0.2$  V larger than P3HT giving evidence that the interface band gap of PCDTBT is  $1.35$ – $1.4$  eV.

#### B. Density of states model

The proposed DOS model for P3HT:PCBM is given in Fig. 15 and is constructed from the  $1.2$ -eV value of the interface band gap, the calculated DOS above the gap, and the slope of the exponential optical absorption for the band tail. A parabolic DOS,  $N(E) \sim (E - E_C)^{1/2}$ , where  $E_C$  is the band-edge energy, is used for both the polymer HOMO and the PCBM LUMO for energies away from the band edges, assumed to be the states of mobile electrons and holes. In the absence of further information we assume the same DOS for both bands and set the DOS equal to that obtained from the first principles calculations in Fig. 14. Near the band edge, the disorder effects are modeled with exponential band tails of localized states. Also lacking further information we make the valence-band (HOMO) band tail broader than the conduction-band (LUMO) tail, implying that the mobility is lower for the polymer than for PCBM. The band tails are constructed to fit smoothly to the band states, as indicated by the calculations shown in Fig. 14. The valence-band tail is given a slope of  $0.037$  eV, being the measured slope of the optical absorption edge for the P3HT cell. The conduction-band tail is given a smaller slope chosen to be  $0.03$  eV, which is a value indicated by PDS measurements.<sup>35</sup> Figure 15 also shows a broader exponential band tail with a smaller DOS denoted  $D(E)$ . This feature is introduced to account for the low absorption region of the spectral response, as discussed below, and is arbitrarily attached to the LUMO band rather than the HOMO. The comparable model for PCDTBT:PC<sub>70</sub>BM has a band gap of  $1.4$  eV and a band tail slope of  $0.045$  eV.

Figure 15 also shows the electron and hole occupancy of the states, calculated as the product  $N(E)F(E)$ , where  $F(E)$  is the Fermi function and the quasi-Fermi energies are set at  $0.3$  eV below the respective band edges. This distribution of carriers

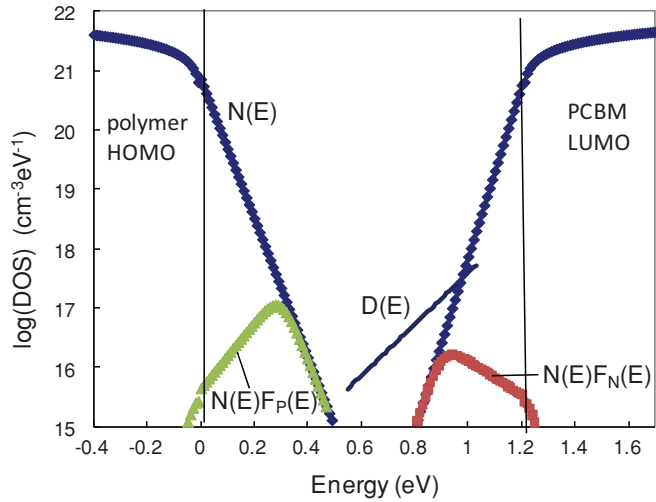


FIG. 15. The proposed model for the DOS  $N(E)$  in P3HT:PCBM, as a function of energy. The model describes the HOMO levels (valence band) of the polymer and the LUMO levels (conduction band) of PCBM. Vertical lines represent the band edges separating mobile states from localized states. The calculated occupancy of the states  $N(E)F_i(E)$ , where  $F_{N,p}(E)$  is the Fermi function for electrons and holes, is shown to illustrate the conditions under 1-sun illumination, assuming quasi-Fermi energies which are 0.3 eV from the band edges. The line marked  $D(E)$  is shown to illustrate a possible additional state distribution used to account for the weak absorption in Fig. 16.

corresponds to  $\sim 1$ -sun illumination. The result shows that the carriers mostly occupy localized states.

### C. Weak-coupling model for optical transitions

Next it is shown that the weak coupling with disorder (WCD) approach for the CT optical transitions, along with the proposed DOS, provides a quantitative model for the optical absorption. The model is one which is applied successfully to virtually all disordered inorganic semiconductors, and which completely neglects both exciton effects and the electron-phonon coupling. The model uses the assumed density of one-electron states, comprising the polymer HOMO,  $N_V(E)$ , and the PCBM LUMO,  $N_C(E)$ , as described in Fig. 15. The absorption is described by an integral over the joint DOS,<sup>36</sup>

$$\alpha_T(\hbar\omega) = cV_F \int \frac{N_V(E)N_C(E + \hbar\omega)|M|^2}{\hbar\omega} dE, \quad (16)$$

where  $\hbar\omega$  is the photon energy,  $M$  is the transition matrix element, and the constant  $c$  is given in Ref. 36. Equation (16) includes a factor  $V_F$  which is the volume fraction of the material associated with the interface transitions. Since absorption is between spatially separate states, there should be no selection rules to forbid transitions, and so a constant matrix element  $M$  is assumed in the calculation of the absorption.

Figure 16 compares the measured and calculated absorption and shows that there is good agreement for the P3HT:PCBM spectrum with the assumed DOS with an interface band gap of 1.2 eV and the valence-band tail slope of 0.037 eV. The absorption calculated from the joint DOS is dominated by the broader of the two band tails, and so the choice of

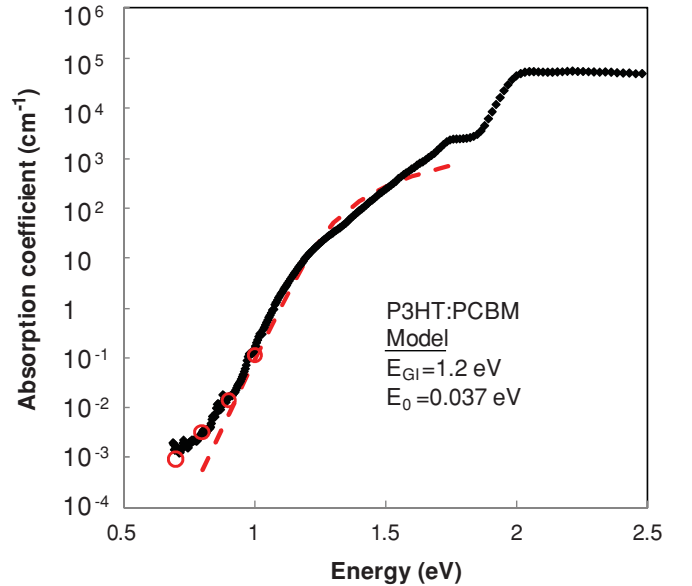


FIG. 16. The measured optical absorption of P3HT:PCBM taken from Fig. 4, compared to the joint DOS calculated from Eq. (16) for the DOS model in Fig. 15. The values used for the interface gap  $E_{GI}$  and the exponential slope  $E_0$  are shown. Open circles include the extra states  $D(E)$  shown in Fig. 15, and the dashed line excludes this contribution.

the conduction-band tail slope hardly affects the result. The open circles in Fig. 16 show the absorption calculation which includes the extra band tail states  $D(E)$  indicated in Fig. 15. This calculation illustrates the possible origin of the change in slope of the weak absorption region.

From the assumptions of parabolic bands, it also follows from Eq. (16) that at energy sufficiently larger than  $E_{GI}$ ,<sup>37</sup>

$$\alpha_T(\hbar\omega)\hbar\omega = c'V_F(E - E_{GI})^2, \quad (17)$$

where  $c'$  is derived from  $c$  and the constants of integration in Eq. (16). This expression gives a reasonable fit to the data above the interface gap although there is not a large enough energy range between  $E_{GI}$  and the bulk band gaps for an accurate measurement of the interface gap from this analysis. The PCDTBT absorption data cover an even smaller energy range.

The interface band gap occurs at an absorption coefficient of  $\sim 10$   $\text{cm}^{-1}$ , while in amorphous inorganic semiconductors for which the WCD model applies well, the bulk band-gap energy generally occurs at an absorption coefficient of  $\alpha_T = 10^3 - 10^4$   $\text{cm}^{-1}$ . The CT absorption strength is reduced by the two factors  $V_F$  and  $M$  in Eq. (16). The interface region comprises a small fraction of the material, and if we assume that the optical transitions involve states within 0.5 nm of the interface, the fraction is  $V_F \sim 0.1$ . The matrix elements  $M$  for the transition are also reduced because the optical transition is between spatially separate states on opposite sides of the interface. The reduction is by an overlap factor such as  $\exp(-2R/R_0)$ , where  $R$  is the separation of the electron and hole and  $R_0$  describes the wave-function penetration into the neighboring domain. The overlap factor can easily account for another factor of 10 in the strength of the absorption. The DOS in the bands also factors into the magnitude of the absorption.

Although these factors are not known accurately, a mobility gap occurring at the energy when  $\alpha = 10 \text{ cm}^{-1}$  is consistent with the expected reduced absorption strength.

#### IV. DISCUSSION

We have shown that the DOS model of Fig. 15 relates the photoconductivity spectrum, the dispersive transport of carriers, and the calculations of the electronic structure for a disordered polycrystalline P3HT. This hypothesis makes several assumptions about the physical mechanisms, for which further experimental support is needed. Some of the information gaps are discussed next.

##### A. Multiple trapping model for the mobility

The most obvious information gap is the identity of the slower carrier in the transient photoconductivity measurements, since the information would determine which band tail to associate with the measured exponential slope. Measurements find that the mobility in PCBM is  $>10^{-3} \text{ cm}^2/\text{V s}$ .<sup>38</sup> The mobility of P3HT in TFTs varies widely from  $10^{-5}$  to  $0.1 \text{ cm}^2/\text{V s}$  depending on the crystalline order.<sup>39</sup> These P3HT values are for the in-plane mobility, and the out-of-plane mobility, involving transitions across lamella planes, should be considerably smaller because of the weak electronic overlap between the lamella planes. The anisotropy of the P3HT mobility and its relation to structural order is well established.<sup>40</sup> Since the solar cell involves out-of-plane transport, we will take as a working hypothesis that the polymer has the lower mobility. More detailed transient photoconductivity measurements should be able to resolve the question and the details of the crystalline orientation of both the polymer and PCBM will be important to understand the transport.<sup>41</sup>

Polymer semiconductors, and P3HT in particular, are used for TFTs, and the TFT characteristics are often described in terms of a DOS distribution with mobile and localized band tail states.<sup>32,42</sup> Typical organic TFTs devices have a significant subthreshold region, corresponding to the range of gate voltages between the turn-on voltage and the threshold voltage. The subthreshold region is usually interpreted as arising from band tail localized states which keeps the Fermi energy away from the band edge. One analysis of poly(quarterthiophene) (PQT), which is closely related to P3HT, found that the TFT data could be explained by a band tail slope of  $0.04 \text{ eV}$ ,<sup>32</sup> similar to the values found in our analysis. The TFT has a different structure and transport path compared to the BHJ solar cells, but does provide support for the band tail interpretation of the absorption and transport data.

##### B. Bulk or interface density of states

The exponential band tail offers a consistent interpretation of the low-energy CT absorption band and the transport of carriers in the BJH structure. However, these two measurements do not necessarily involve the same states. The CT optical absorption is confined to the interface region of the BHJ structure while the charge transport is a bulk property of each domain. The distinction between bulk and interface is blurred in a BHJ structure because of the small domain size.

The carrier transport could be dominated by specific interface states, since the diffusion length is sufficient that the carrier will interact frequently with the interface during the transit. Alternatively the DOS may represent the bulk values for which the absorption only samples the fraction of those states that are near the interface. Thus it cannot be determined yet whether the DOS model is characteristic of the domain bulk or the interface region in the BHJ devices. The model in Fig. 15 describes a bulk distribution of states.

The physical nature of the band tail states also remains to be determined. In addition to localized states arising from grain boundaries and amorphous disorder, the structural disorder of the BHJ interface can introduce localization at a mesoscopic scale. The development of an empirical DOS helps separate the question of the physical origin of the states from the question of their role in the electronic properties of the solar cell.

In recent publications,<sup>34,43</sup> we have shown that these BHJ solar cells exhibit first order recombination kinetics below 1-sun illumination levels. We argued that the most likely mechanism is Shockley-Read-Hall recombination through localized states in the gap, at or near the BHJ interface. The DOS that we develop in Fig. 15 has localized states that are consistent with the proposed recombination mechanism, corresponding to transitions between mobile PCBM electrons and band tail polymer holes, and/or between mobile holes and trapped electrons.

##### C. Phonon interactions and the CT exciton energy

Our analysis finds that the WCD model can account for the CT optical absorption with a DOS model that is consistent with calculations and with the transient photoconductivity data. Vandewal *et al.* recently show that the SC model also accounts for the CT absorption, assuming a single CT energy broadened by electron-phonon interactions.<sup>12</sup> According to the SC model, the shape of the low-energy absorption is dominated by the electron-phonon interactions, to form a Gaussian band. Their analysis of P3HT:PCBM finds a zero phonon energy for the CT transition of  $1.14 \text{ eV}$  at room temperature, with a peak of the CT band at  $1.41 \text{ eV}$ , and a phonon coupling energy of  $\lambda = 0.27 \text{ eV}$ . The zero phonon energy found from the SC model is sufficiently similar to the interface gap obtained from the WCD model that the two models cannot be separated from this energy alone.

The SC model attributes the band-edge absorption to a CT exciton transition, and the zero phonon exciton energy  $E_X$  is always lower than the one-electron band gap by the exciton binding energy. Vandewal *et al.*<sup>12</sup> show that the temperature dependence of the CT absorption band gives a similar low-temperature extrapolated energy as that obtained from temperature measurements of  $V_{OC}$ , which is expected to have the form

$$V_{OC}(T) = E_{GI} - \text{const}kT. \quad (18)$$

Equation (18) is closely related to Eq. (15). Since  $V_{OC}(T)$  extrapolates to the one-electron band gap  $E_{GI}$ , the comparison suggests that  $E_X \sim E_{GI}$ , so that the exciton binding energy is small. Other solar cell studies also indicate that the CT exciton at the interface is not strongly bound.<sup>3,4</sup> The explanation

for the weak binding energy is that electron and hole states are separated on either side of the interface and hence must have smaller Coulomb energy than excitons in the bulk.<sup>4</sup> The uncertainty in the parameters allows for an exciton binding energy at least up to 0.1 eV, but 0.3 eV seems too large to be consistent with the data. The SC model does not imply any particular exciton binding energy, although it is generally the case that strongly coupled excitons have large binding energy.

The phonon interactions are harder to assess since both models fit the band-edge absorption. The problem is that the electron-phonon interaction moves the absorption strength to higher energy, but the WCD model accounts for the higher absorption by the increasing DOS in the band. Both models therefore predict a broad absorption band. Two further points are as follows:

(1) The SC model explains the broad low-energy electroluminescence spectra that Vandewal *et al.* observe,<sup>12</sup> since the emission should be below the absorption peak by the Stokes shift. The WCD interpretation of the data is that the luminescence energy and width arises at least in part from thermalization of carriers down the band tails so that the recombination transitions are between low-energy states in the band tail distribution.

(2) The optical absorption of bulk polymers usually shows structure associated with the phonon sidebands of the phonon-coupled exciton absorption transitions. For example, the P3HT:PCBM cell shows such structure between 2 and 2.5 eV. However, the CT optical absorption does not show any visible phonon sidebands over a fairly wide energy range.

#### D. Band offsets and band-edge energies

Finally we consider what information the measurements give about the band offsets. The band offset between the two materials of the BHJ cell provides the energy to split optically excited excitons into mobile free carriers. The offset must be large enough to split the exciton, but small enough that the open-circuit voltage is not reduced more than necessary by the energy reduction that accompanies CT.

The separation of the bulk optical absorption at  $\sim 1.9$  eV and the interface gap is  $\sim 0.7$  eV in the P3HT cell (see Fig. 4), giving a measure of the effective band offset. We refer to this as an effective band offset because the optical absorption edge in the bulk polymer is dominated by an exciton transition, and does not necessarily correspond to the one-electron band gap, which may be at higher energy than the onset of strong absorption. The effective band offset is important for the solar cell performance because the difference between  $E_{GI}$  and the absorption edge represents the loss of solar response arising from the exciton splitting. In the PCDTBT cell, the separation between the interface gap and the optical absorption edge is smaller by 0.25–0.3 eV compared to the P3HT cell, and hence the effective band offset is 0.4–0.5 eV. The reduced offset is one reason why the PCDTBT cell has higher solar cell efficiency. Ideally the effective band offset should be much smaller.

The two cells studied here have different donor and acceptor materials, and so we cannot draw any conclusion about the

relative HOMO levels of the two polymers or the LUMO levels of the two types of PCBM. However, if photoconductivity spectrum measurements were made on cells that share a common material, then the shift of the interface gap should directly reflect the difference in the HOMO of two donors or the LUMO of two acceptors. Given a set of cells made with various different materials, it should be possible to obtain the relative energy levels of the HOMO and LUMO levels of each material and to identify if there are any chemical interactions that modify the interface energy.

#### V. SUMMARY

This work describes information about the electronic structure of BHJ solar cells, based on measurements of the photoconductivity spectral response and carrier mobility, and theoretical calculations. Evidence is presented for band tail states with an approximately exponential DOS, with a similar slope obtained by both experiments and consistent with the theory. However, we are not yet able to determine with certainty which band tail is being measured. The measurements conclude that the interface band gap—the separation of the polymer HOMO and the PCBM LUMO—occurs at an absorption coefficient of  $\sim 10 \text{ cm}^{-1}$  in the spectral response data and may offer a method to obtain the same information for other BHJ solar cells. The data is used to develop a DOS model, although several aspects of the model are as yet undetermined.

We show that the photoconductivity spectral response can be explained by a model of weak phonon coupling with disorder-induced band tail states, based on the proposed DOS. This approach contrasts with a strong phonon coupling model that also accounts for the general shape of the spectral response. At present we are unable to distinguish unambiguously between the two models. It is likely that both band tail states and phonon coupling are significant.

Transient photoconductivity measures the combination of the electron and hole transport, and while we can identify and separate the two components, we cannot yet tell which is which. We develop an analytical procedure to obtain the dispersion parameter and the mobility from the experimental data. The slower of the two carriers is dispersive with room-temperature mobility  $\sim 10^{-4} \text{ cm}^2/\text{V s}$ . The mobility is thermally activated and has a temperature-dependent dispersion parameter that is consistent with multiple trapping in an exponential band tail.

#### ACKNOWLEDGMENTS

We would like to thank A. Salleo for helpful discussions about polymer structure and C. Paulson for technical assistance. Research at PARC was partially supported in part by AFOSR Grant No. FA9550-09-1-0436. Research at UCSB was supported as part of the Center for Energy Efficient Materials, an Energy Frontier Research Center funded by the US Department of Energy, Office of Science, Office of Basic Energy Sciences.



- <sup>1</sup>S. Gunes, H. Neugebauer, and N. S. Sariciftci, *Chem. Rev.* **107**, 1324 (2007).
- <sup>2</sup>J.-L. Bredas, J. Cornil, and A. J. Heeger, *Adv. Mater. (Weinheim, Ger.)* **8**, 447 (1996).
- <sup>3</sup>M. Hallermann, S. Haneder, and E. Da Como, *Appl. Phys. Lett.* **93**, 053307 (2008).
- <sup>4</sup>R. A. Street, *Appl. Phys. Lett.* **93**, 133308 (2008).
- <sup>5</sup>H. Bassler, *Phys. Status Solidi B* **175**, 15 (1993).
- <sup>6</sup>F. W. Schmidlin, *Phys. Rev. B* **16**, 2362 (1977); B. Hartenstein, H. Bassler, A. Jakobs, and K. W. Kehr, *ibid.* **54**, 8574 (1996).
- <sup>7</sup>PCDTBT is poly(N-9'-hepta-decanyl-2,7-carbazole-alt-5,5-(4',7'-di-2-thienyl-2',1',3'-benzothiadiazole); PC(70)BM is [6-6]-phenyl C61(70)-butyric acid methyl ester; P3HT is poly(3-hexylthiophene).
- <sup>8</sup>N. Blouin, A. Michaud, and M. LeClerc, *Adv. Mater. (Weinheim, Ger.)* **19**, 2295 (2007).
- <sup>9</sup>J. Y. Kim, S. H. Kim, H.-H. Lee, K. Lee, W. Ma, X. Gong, and A. J. Heeger, *Adv. Mater. (Weinheim, Ger.)* **18**, 572 (2006).
- <sup>10</sup>L. Goris, A. Poruba, L. Hodakova, M. Vanacek, K. Haenen, M. Nesladek, P. Wagner, D. Vandezande, L. De Schepper, and J. V. Manca, *Appl. Phys. Lett.* **88**, 052113 (2006).
- <sup>11</sup>K. Vandewal, L. Goris, I. Haeldermans, M. Nesladek, K. Haenan, P. Wagner, and J. V. Manca, *Thin Solid Films* **516**, 7135 (2008).
- <sup>12</sup>K. Vandewal, K. Tvingstedt, A. Gadisa, O. Inganäs, and J. V. Manca, *Phys. Rev. B* **81**, 125204 (2010).
- <sup>13</sup>J. J. Benson-Smith, L. Goris, K. Vandewal, K. Haenan, J. V. Manca, D. Vandezande, D. D. C. Bradley, and J. Nelson, *Adv. Funct. Mater.* **17**, 451 (2007).
- <sup>14</sup>J. Lee, K. Vandewal, S. R. Yost, M. E. Bahlke, L. Goris, M. A. Baldo, J. V. Manca, and T. Van Voorhis, *J. Am. Chem. Soc.* **132**, 11878 (2010).
- <sup>15</sup>S. H. Park, A. Roy, S. Beaupre, S. Cho, N. Coates, J. S. Moon, D. Moses, M. Leclerc, K. Lee, and A. J. Heeger, *Nat. Photon.* **3**, 297 (2009).
- <sup>16</sup>F. Urbach, *Phys. Rev.* **92**, 1324 (1953); see also Ref. 36.
- <sup>17</sup>G. D. Cody, T. Tiedje, B. Abeles, B. Brooks, and Y. Goldstein, *Phys. Rev. Lett.* **47**, 1480 (1981).
- <sup>18</sup>N. Karl, K.-H. Kraft, J. Marktanner, M. Munch, F. Schatz, R. Stehle, and H.-M. Uhde, *J. Vac. Sci. Technol. A* **17**, 2318 (1999).
- <sup>19</sup>C. R. McNeill and N. C. Greenham, *Appl. Phys. Lett.* **93**, 203310 (2008).
- <sup>20</sup>S. A. Choulis, Y. Kim, J. Nelson, D. D. C. Bradley, M. Giles, M. Shkunov, and I. McCulloch, *Appl. Phys. Lett.* **85**, 3890 (2004).
- <sup>21</sup>M. Punke, S. Valouch, S. W. Kettlitz, N. Christ, C. Gartner, M. Gerken, and U. Lemmer, *Appl. Phys. Lett.* **91**, 071118 (2007).
- <sup>22</sup>J. M. Marshall, H. Michiel, and G. J. Adriaenssens, *Philos. Mag. B* **47**, 211 (1983).
- <sup>23</sup>R. A. Street, S. Cowan, and A. J. Heeger, *Phys. Rev. B* **82**, 121301 (2010).
- <sup>24</sup>S. R. Cowan, R. A. Street, S. Cho, and A. J. Heeger, *Phys. Rev. B* **83**, 035205 (2011).
- <sup>25</sup>H. Scher and E. W. Montroll, *Phys. Rev. B* **12**, 2455 (1975).
- <sup>26</sup>T. Tiedje and A. Rose, *Solid State. Commun.* **37**, 49 (1980).
- <sup>27</sup>L. H. Jimison, M. F. Toney, I. McCulloch, M. Heeney, and A. Salleo, *Adv. Mater. (Weinheim, Ger.)* **21**, 1568 (2009).
- <sup>28</sup>J. Rivnay, R. Noriega, J. E. Northrup, J. Kline, M. F. Toney, and A. Salleo, *Phys. Rev.* (submitted).
- <sup>29</sup>J. E. Northrup, *Phys. Rev. B* **76**, 245202 (2007).
- <sup>30</sup>D. M. DeLongchamp, R. J. Kline, E. K. Lin, D. A. Fischer, L. J. Richter, L. A. Lucas, M. Heeney, I. McCulloch, and J. E. Northrup, *Adv. Mater. (Weinheim, Ger.)* **19**, 833 (2007).
- <sup>31</sup>R. A. Street, *Hydrogenated Amorphous Silicon* (Cambridge University Press, Cambridge, UK, 1991).
- <sup>32</sup>A. Salleo, T. W. Chen, A. R. Volkel, Y. Wu, P. Liu, B. S. Ong, and R. A. Street, *Phys. Rev. B* **70**, 115311 (2004).
- <sup>33</sup>L. J. A. Koster, V. D. Mihailetschi, and P. W. M. Blom, *Appl. Phys. Lett.* **88**, 093511 (2006); M. C. Scharber, D. Muhlbacher, M. Koppe, P. Denk, C. Waldauf, A. J. Heeger, and C. J. Brabec, *Adv. Mater. (Weinheim, Ger.)* **18**, 789 (2006); J. Hou, T. L. Chen, S. Zhang, L. Huo, S. Sista, and Y. Yang, *Macromolecules* **42**, 9217 (2009); C.-W. Chu, V. Shrotriya, G. Li, and Y. Yang, *Appl. Phys. Lett.* **88**, 153504 (2006).
- <sup>34</sup>R. A. Street, M. Schoendorf, A. Roy, and J. H. Lee, *Phys. Rev. B* **81**, 205307 (2010).
- <sup>35</sup>A. Salleo (private communication).
- <sup>36</sup>N. F. Mott and E. A. Davis, *Electronic Processes in Non-crystalline Materials* (Oxford University Press, Oxford, UK, 1979), p. 289.
- <sup>37</sup>J. Tauc, in *The Optical Properties of Solids*, edited by F. Abeles (North-Holland, Amsterdam, 1970), p. 277.
- <sup>38</sup>H. Yokoyama, E. J. Kramer, M. H. Rafailovich, J. Sokolov, and S. A. Schwarz, *Macromolecules* **31**, 8826 (1998).
- <sup>39</sup>H. Sirringhaus, P. J. Brown, R. H. Friend, M. M. Nielsen, K. Bechgaard, B. M. W. Lanveld-Voss, A. J. H. Spiering, R. A. J. Janssen, E. W. Meijer, P. Herwig, and D. M. de Leeuw, *Nature (London)* **401**, 685 (1999); also R. J. Kline, M. D. McGehee, E. N. Kadnikova, J. Liu, and J. M. J. Frechet, *Adv. Mater. (Weinheim, Ger.)* **15**, 1519 (2003).
- <sup>40</sup>L. H. Jimison, M. F. Toney, I. McCulloch, M. Heeney, and A. Salleo, *Adv. Mater. (Weinheim, Ger.)* **21**, 1568 (2009).
- <sup>41</sup>X. Yang, J. K. J. van Duren, M. T. Rispens, J. C. Hummelen, R. A. J. Janssen, M. A. J. Michels, and J. Loos, *Adv. Mater. (Weinheim, Ger.)* **16**, 802 (2004).
- <sup>42</sup>D. Oberhoff, K. Pernstich, D. J. Gundlach, and B. Batlogg, *IEEE Trans. Electron Devices* **54**, 17 (2007).
- <sup>43</sup>R. A. Street, *Phys. Rev. B* **82**, 207302 (2010).